

Acoustic-gravity waves from the source region of the 2011 great Tohoku earthquake ($M_w = 9.0$)

Takeshi Mikumo,¹ Milton Garces,² Takuo Shibutani,³ Wataru Morii,³ Takashi Okawa,⁴ and Yasushi Ishihara⁵

Received 5 February 2013; revised 27 February 2013; accepted 1 March 2013; published 22 April 2013.

[1] Atmospheric pressure waves were recorded within 5 h after the 2011 great Tohoku earthquake ($M_w = 9.0$) by sensitive microbarographs at four regional stations and eight International Monitoring System stations at distances up to 6700 km. While its apparent phase velocity between the regional stations is 341 m/s, the global stations indicate weak dispersive wave trains with low frequencies between 1.6 and 4.8 mHz, propagating with an average phase velocity around 364 m/s. The low-frequency waves may be interpreted as acoustic-gravity waves excited by upheaval and depression of the sea surface in the source region due to coseismic uplift and subsidence of the sea bottom during this great thrust earthquake. Assuming the source dimension and the average coseismic vertical displacements of the sea surface, with reference to tsunami observations, we calculate synthetic waveforms for some of the far-field stations by incorporating a standard sound velocity structure in the atmosphere up to an altitude of 220 km. The synthetics provide reasonable explanations for the general features of the observed waveforms, suggesting possible ranges for the source parameters generating these acoustic-gravity waves. Our analysis suggests that the average initial upheaval of the sea surface in the central zones of the source region may exceed 4–6 m and that the risetime of the coseismic deformation may be in the range between 3 and 4 min. In the eastern narrow zone adjacent to the Japan Trench, the deformation has significantly higher initial amplitude and shorter risetime.

Citation: Mikumo, T., M. Garces, T. Shibutani, W. Morii, T. Okawa, and Y. Ishihara (2013), Acoustic-gravity waves from the source region of the 2011 great Tohoku earthquake ($M_w = 9.0$), *J. Geophys. Res. Solid Earth*, 118, 1534–1545, doi:10.1002/jgrb.50143.

1. Introduction

[2] The great earthquake ($M_w = 9.0$) took place off the Pacific coast of the Tohoku region, northeast Japan (38.103°N, 142.861°E at 05:46:23 UTC) (Japan Meteorological Agency) on 11 March 2011. The earthquake caused extremely strong ground motion and large tectonic ground deformations near the coast and inland regions, as well as unusually high tsunami inundation, which brought heavy damage in and around the Tohoku region. A large number of data from tsunami observations with coastal tide gauges, offshore ocean-bottom pressure gauges, and GPS wave gauges revealed the extent of tsunami source region and sea-surface

displacements [Fujii *et al.*, 2011; Hayashi *et al.*, 2011; Maeda *et al.*, 2011; Sato *et al.*, 2011; Saito *et al.*, 2011; Gusman *et al.*, 2012]. Long-period seismic waves recorded at near- and far-field stations, sometimes with geodetic data, also provided estimates on fault slip, fault dimension, and rupture propagation process [e.g., Yagi and Fukahata, 2011; Ide *et al.*, 2011; Yoshida *et al.*, 2011; Lay *et al.*, 2011; Koketsu *et al.*, 2011; Ammon *et al.*, 2011; Lee *et al.*, 2011]. From the tsunami and seismic data analysis, the source region of this great thrust earthquake was estimated as extending for 400–550 km long in the NS direction and about 200 km wide in the EW direction, with a maximum fault slip of 40–50 m near the Japan Trench, where the Pacific plate subducts beneath northeast Japan from the east side.

[3] Besides these observations, low-frequency atmospheric pressure waves were recorded within 5 h after the earthquake by sensitive microbarographs not only at four regional, near-field stations on the Japanese Islands and in Korea but also at eight global International Monitoring System (IMS) stations in the distance range between 1100 and 6700 km. Similar observations of this type of low-frequency pressure waves have been reported in the cases of the 1964 Alaskan earthquake ($M_w = 9.2$) [Bolt, 1964; Mikumo, 1968] and the 2004 Sumatra-Andaman earthquake ($M_w = 9.2$) [Mikumo *et al.*, 2008].

[4] In the present article, we summarize the evidence for low-frequency acoustic-gravity waves propagating from the

Additional supporting information may be found in the online version of this article.

¹Kyoto University, Uji, Kyoto, Japan.

²Infrasound Laboratory, University of Hawaii, Kailua-Kona, Hawaii, USA.

³Disaster Prevention Research Institute, Kyoto University, Uji, Kyoto, Japan.

⁴Seismological Observatory, Japan Meteorological Agency, Matsushiro, Nagano, Japan.

⁵Japan Agency for Marine-Earth Science and Technology, Yokohama, Japan.

Corresponding author: T. Mikumo, Kyoto University, Uji, Kyoto 611-0002, Japan. (mikumo@maia.eonet.ne.jp)

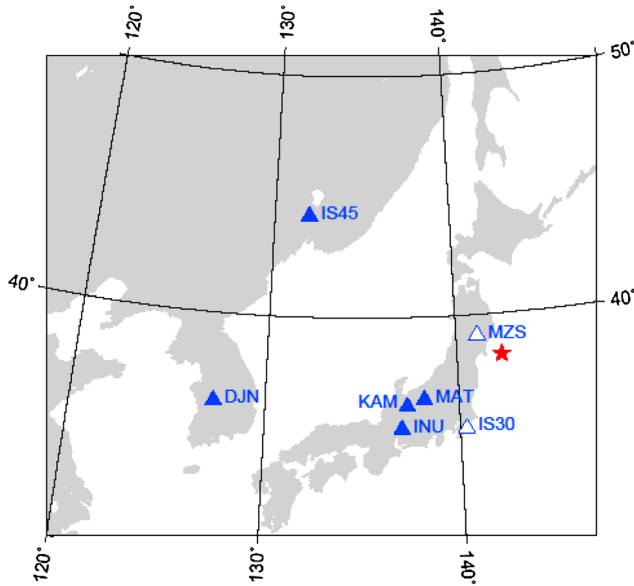


Figure 1. Locations of regional stations that recorded atmospheric pressure waves after the 2011 great Tohoku earthquake: asterisk, JMA epicenter; solid triangles, regional stations dealt with in this article; open triangles, regional stations mentioned in *Arai et al.* [2011].

source region to a number of microbarograph stations through the lower to middle atmosphere. We also calculate their synthetic waveforms, referring to the tsunami and seismic data described above, and then compare the synthetics with the corresponding observations. Our main purpose here is to estimate the overall source characteristics for effectively generating the acoustic-gravity waves, which would provide independent information on the source characteristics of this great earthquake.

2. Observations

[5] Low-frequency atmospheric pressure waves have been recorded at both regional and global stations. Station locations are shown in Figures 1 and 2, and their coordinates and epicentral distances and the observed results are summarized in Table 1. The original microbarograph records at these stations are sometimes contaminated by atmospheric ambient noise and daily disturbances prevailing in regions around these stations. We apply a second-order Butterworth band-pass filter with a unit amplitude to all these records over a frequency range between 1.19 and 8.33 mHz (or between 14 and 2 min) to extract signals of propagating acoustic-gravity waves, removing all disturbances outside these frequencies. The reason for our choice of the frequency range comes from the dynamic response of the lower atmosphere [Harkrider, 1964], following a similar procedure taken in previous studies of the 1964 Alaskan earthquake [Mikumo, 1968] and the 2004 Sumatra-Andaman earthquake [Mikumo et al., 2008].

2.1. Regional Stations

[6] The pressure waves were recorded at three regional, near-field stations on the Japanese Islands and another station in Korea. The nearest station here (447 km) is the Matsushiro Seismological Observatory (MAT), Japan Meteorological

Agency (JMA), where two channel records have been obtained, indicating coherent signals. The second one is the Kamioka station (KAM) operated by the Disaster Prevention Research Institute, Kyoto University, which provided a single-channel record. The microbarographs used at these stations have a flat frequency response from 0.5 Hz to DC, and the rate of data sampling is 1 Hz. The third station, i.e., Inuyama (INU), located at the Seismological Observatory, Nagoya University, and the fourth station, i.e., Daejeon (DJN), in southern Korea, both of which are operated by the Japan Agency for Marine-Earth Science and Technology (JAMSTEC), have a similar flat frequency response and a data resolution of 0.02 Pa, each providing a single-channel record, respectively. Because these original records include daily pressure variations, they have been detrended before applying the band-pass filtering. The filtered waveforms in this way for the four stations are shown in Figures 3a and 3b. The maximum peak-to-peak amplitudes at these stations are nearly the same around 14–17 Pa (Table 1). The first arrivals recorded at these stations show group velocities ranging between 301 and 328 m/s (from the JMA epicenter) and indicate an apparent phase velocity of 341 m/s between the nearest and farthest stations, as shown in Figure 5a. Looking at the filtered records at the four stations, we notice successive three or four wave trains with large amplitudes and periods between 4 and 7 min within the time of about 1800 s (30 min) (for a longer time interval, see Supplementary Figures RS in the supporting information). Although we cannot locate exactly at this moment where these trains came from, there is a possibility that these could be multiply-reflected waves between a boundary somewhere between the stratosphere or the mesosphere and

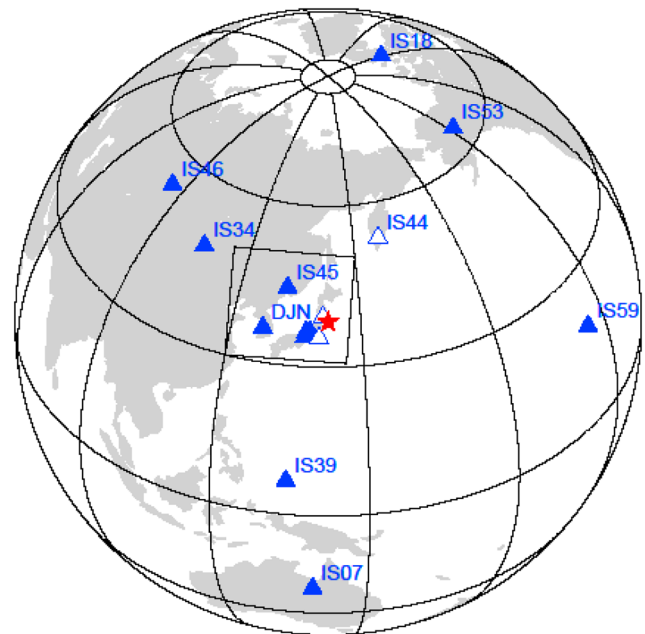


Figure 2. Locations of global IMS stations that recorded atmospheric pressure waves after the 2011 great Tohoku earthquake: asterisk, JMA epicenter; solid triangles, global IMS stations dealt with in this paper; open triangles, stations not used in this paper. Stations enclosed by a square indicate regional stations shown in Figure 1.

Table 1. Locations of Barograph Stations and Summary of Observed Results^a

Stations	Latitude (°N)	Longitude (°E)	Distance r_0 (km)	Azimuth (deg)	Arrival Time (h : m : s)	Maximum Peak-to-Peak Amplitude (Pa)	
IS07	WRA	-19.935	139.325	6429.5	183.9	10:47	0.4
IS18	QNK	77.478	-89.291	6715.7	11.4	10:48	4.0
IS34	MNG	47.812	106.403	3131.6	301.9	08:00	0.8
IS39	PAL	7.536	134.547	3485.7	196.0	08:38	1.0
IS45	USR	44.200	131.977	1136.0	310.0	06:41	3.2
IS46	ZLS	53.949	84.819	4676.8	311.5	09:25	0.8
IS53	FRB	64.875	-147.861	5288.4	32.8	09:54	1.0
IS59	HWI	19.591	-155.894	6200.7	91.1	10:41	2.0
RE01	MAT	36.540	138.210	447.3	248.6	06:11:10	14.0
RE02	KAM	36.280	137.330	531.1	249.3	06:14:39	15.0
RE03	INU	35.350	137.029	603.8	241.4	06:17:42	17.0
RE04	DJN	35.330	127.340	1418.8	262.2	06:58:39	15.0

^aThe distance r_0 is measured from the JMA epicenter, and the station azimuth is measured clockwise at the epicenter from the north.

the ground surface, rather than due to sudden displacement discontinuities in the tsunami source region.

[7] In addition to these regional stations, *Arai et al.* [2011] identified the arrival of atmospheric pressure disturbances on the original records from Mizusawa (MZS) at the National Astronomical Observatory and IS30 (Isumi) stations in the near field. Including also the original records from two other IMS stations, i.e., IS45 (Ussuriysk) and IS44 (Petropavlovsk-Kamchatsky), they interpreted these arrivals with group velocities between 282 and 307 m/s as nondispersive boundary waves propagated along the bottom boundary of the atmosphere [e.g., Watada, 2009]. We do not incorporate IS30 and IS44 stations in this article, however, because our filtered data show that the waveforms recorded at their array sensors are not always coherent, and hence, its arrival time of signals cannot be exactly estimated.

2.2. Global IMS Stations

[8] Atmospheric pressure waves can be also identified at the following eight global IMS stations: IS45 (Ussuriysk, Far East Russia), IS34 (Songino, Mongolia), IS39 (Palau), IS46 (Zalesovo, Central Russia), IS53 (Fairbanks, AK), IS59 (Hawaii), IS07 (Warramunga, Australia), and IS18 (Quanaak, Greenland). All these IMS stations have sensor arrays with an aperture of about 2 km and a flat frequency response over the frequency range between 0.02 and 8 Hz [Garcés et al., 2005; Le Pichon et al., 2010], but decaying toward lower frequencies with a rate of -20 dB/decade. The sampling rate of the IMS infrasonic data is 20 Hz. The locations of the stations are shown in Figure 2, and their coordinates and the epicentral distances are given in Table 1. *Garcés et al.* [2011] identified infrasonic signals in the 0.005–0.1 frequency band from the infrasound arrays in Hawaii by using consistency and correlation between several channels, RMS amplitude, and arriving azimuth and speed and suggested that the signals may have propagated at a very high velocity from the source.

[9] The original data obtained at these global stations have been also detrended and then applied by the same band-pass filtering. The filtered records generally include some noise (as shown in the Supplementary Figures GS for a long time interval) before the arrival of expected wave signals. The essential parts of wave arrival are shown in Figures 4a–4h in the order of their epicentral distances. For stations IS45 (Figure 4a), IS59 (Figure 4f), IS18 (Figure 4h), and, possibly,

IS53 (Figure 4e), the wave train of long periods with several minutes can be well identified following some noise and with rather good coherency between all channels. It is not always easy at other four stations to identify the exact first arrival time

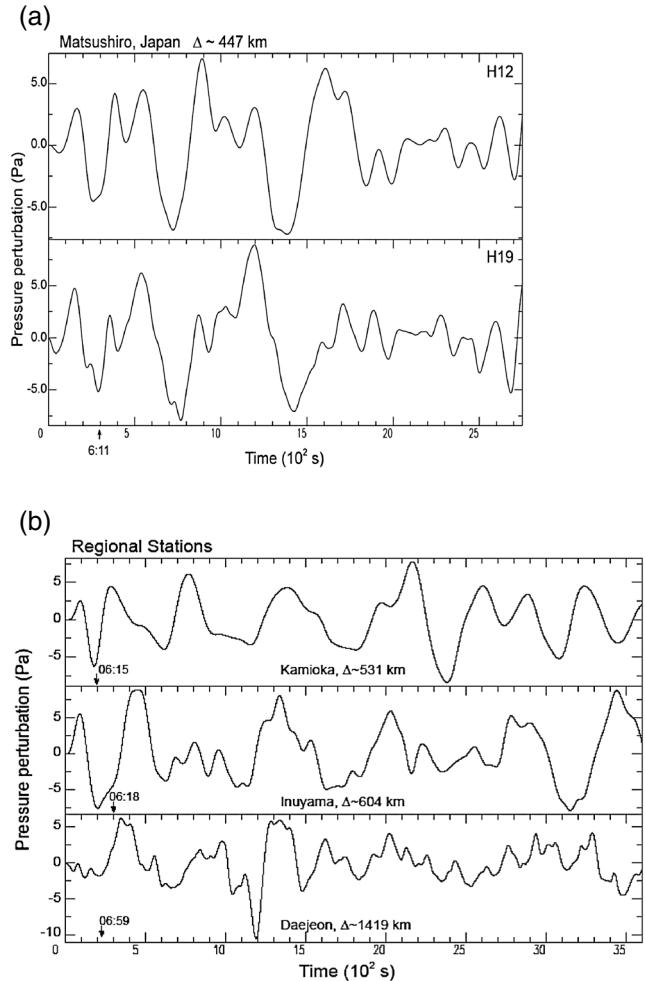


Figure 3. Atmospheric pressure waves recorded at four regional stations: (a) MAT and (b) KAM, INU, and DJN. All the records are band-pass-filtered from their original barograms (see text). Approximate arrival times of the first arrival are indicated in the figures (see also Table 1).

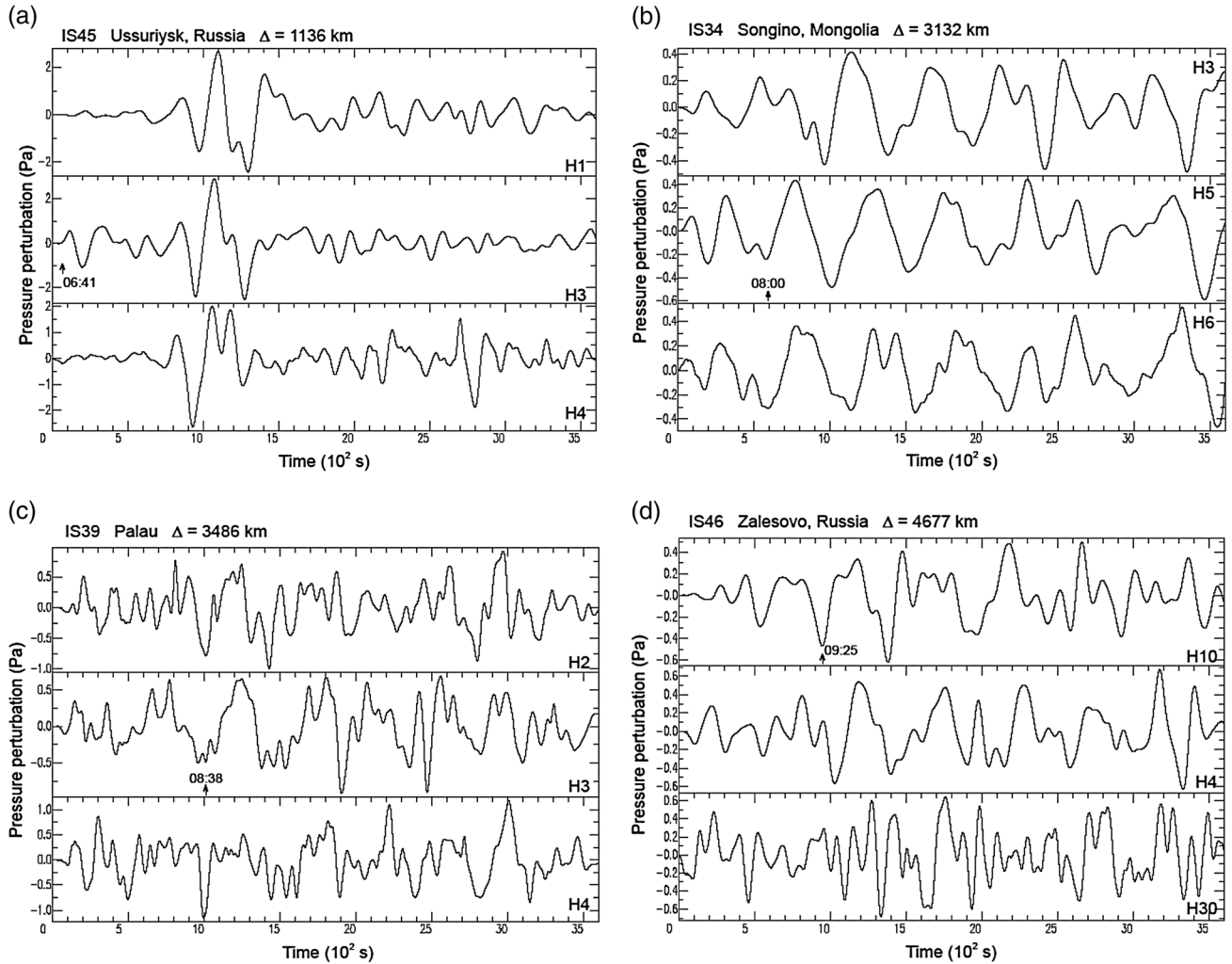


Figure 4. Atmospheric pressure waves recorded at eight global IMS stations in the order of their epicentral distance: (a) IS45 (Ussuriysk), (b) IS34 (Songino, Mongolia), (c) IS39 (Palau), (d) IS46 (Zalesovo), (e) IS39 (Palau), (f) IS53 (Fairbanks), (g) IS59 (Hawaii), (h) IS07 (Warramunga), and (i) IS18 (Quanaak). The records from three or four array sensors at each station are shown, and all the records are band-pass-filtered from their original barograms (see text). Approximate arrival times of the first arrival are also indicated (See Table 1).

of the pressure waves from the records contaminated by the preceding noise. Even in these cases, however, it is not impossible to identify the arrival by looking carefully at their coherency of the low-frequency waveforms, at least between two channels around the expected time of signal arrival. Synthetic waveforms calculated in a later section can help in the identification of signal arrival in these somewhat noisy records. Table 1 thus gives their approximate arrival times, which are subject to an error of 1 min or so.

[10] Figure 5 (b) shows a travel time–distance relation in this distance range. If this relation can be expressed approximately by a straight line, the apparent phase velocity would be about 364 m/s. The high velocity may be explained by propagation of acoustic modes, as mentioned in section 3.1.

[11] We notice that the filtered waveforms shown in Figure 4a for IS45, Figure 4f for IS59, and Figure 4h for IS18 are predominant by relatively shorter periods down to 3 min, while the waveforms at the other five stations involve longer periods even up to 11 min, in spite that the same

band-pass filter has been applied. There is a possibility that the waves at the first three stations appear to involve much energy of the acoustic modes but do not include much of the signals from gravity modes.

[12] Although coherent waveforms can be well identified at station IS45, this station is located in the near field at a distance of about 1100 km from the epicenter, which is not very far as compared with the largest source dimension of 500 km. Since our theory may be applicable to the far field, this station is not included in the waveform modeling. Because the filtered waveforms at station IS39 are considerably contaminated by noise, this station is also not included in the waveform modeling described below.

3. Waveform Modeling

[13] Now we perform waveform modeling for the above filtered waveforms to confirm that the recorded waves can be interpreted as low-frequency acoustic-gravity waves propagating through the atmosphere from the source region

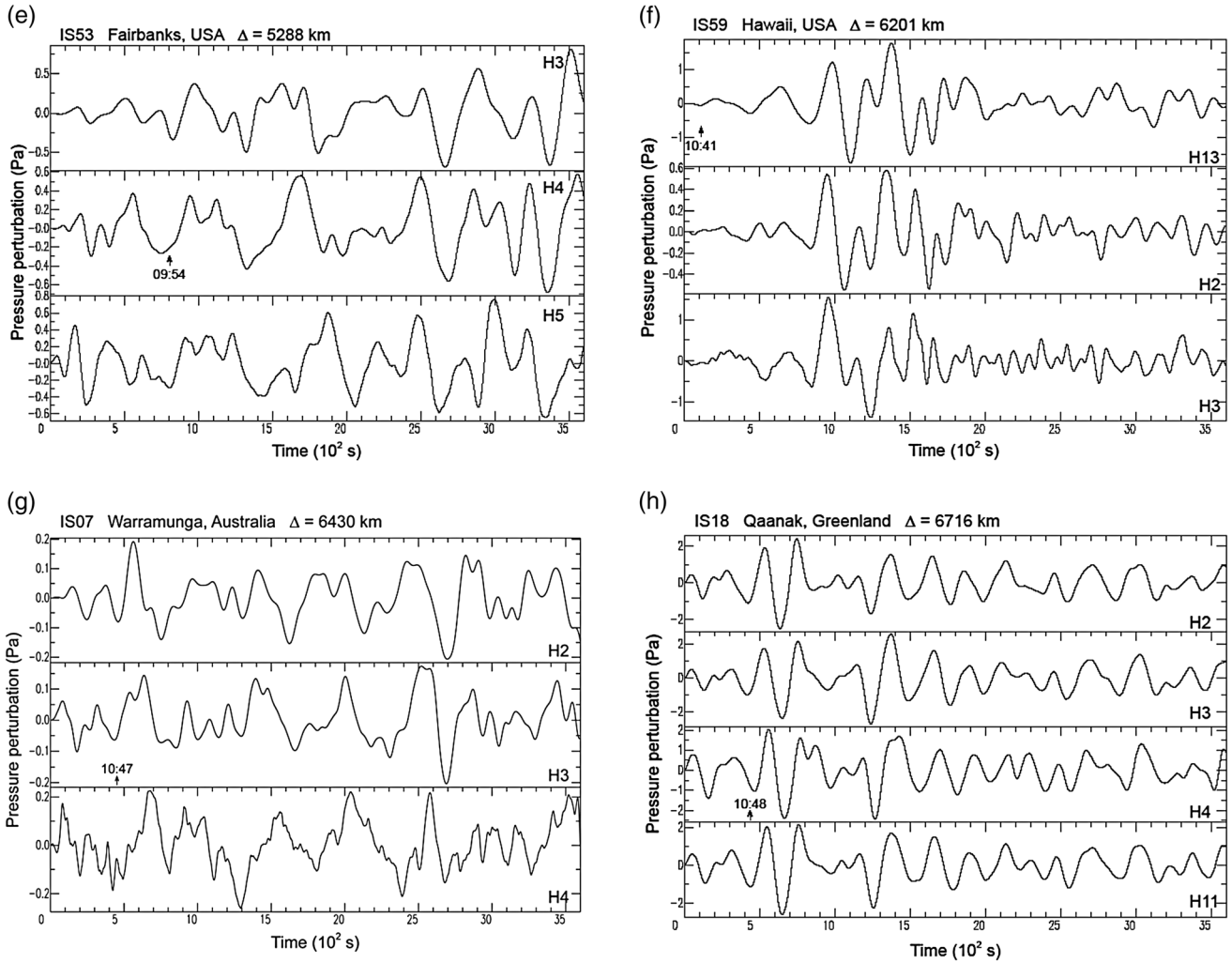


Figure 4. (Continued)

of the 2011 earthquake. A sophisticated way for this purpose would be to apply a normal-mode theory for the solid earth, the ocean, and the atmosphere as a whole system [e.g., Lognonné, 2010; Watada and Kanamori, 2010], but we simply assume here a linear system coupled between the three different media and deal with them separately. To do this, we calculate a large number of synthetic waveforms by forward modeling for each station, incorporating the dynamic response and the temperature and sound velocity structure of the lower to middle atmosphere, and taking into account various source parameters inferred from tsunami and seismic observations described below.

[14] We expect that the source properties still undetermined in different studies to date could be more elucidated by comparing the synthetics with the recorded waveforms.

3.1. Propagation of Acoustic-Gravity Waves in the Lower to Middle Atmosphere

[15] A realistic thermal structure in the lower to middle atmosphere has been established in the early 1960s as the Arnold Research and Development Center (ARDC) model [Wares et al., 1960] and later as the U.S. standard velocity structure. The model has two velocity minima, at altitudes

of about 15 km between the troposphere and the stratosphere and at about 85 km between the mesosphere and the thermosphere, above which the sound velocity increases rapidly even up to 0.7–0.8 km/s at 220 km [e.g., Watada and Kanamori, 2010]. Later and recent models CIRA [Yeh and Liu, 1974], MSISE [Hedin, 1991], and NRL-G2S [Drob et al., 2003] are generally consistent with the standard structure below this altitude. The latest NRL-G2S model covers a detailed velocity structure of the lower atmosphere below 110 km and may be suitable for studying high-frequency waves affected by local and regional structures. We need, however, a more global-scale structure to discuss lower-frequency waves. For the ARDC model, Press and Harkrider [1962] and Pfeffer and Zarichny [1963] calculated the phase and group velocities of acoustic and gravity waves propagating in this range of the atmosphere, assuming that the air density decreases exponentially with altitude. In addition, Harkrider [1964] also computed the dynamic response of the atmosphere to a surface source and receiver by approximating the thermal structure by 39 isothermal, horizontally-stratified layers terminated either with an isothermal half-space or with the free surface at an altitude of 220 km (see Figure S1). In the present article, we refer to the former

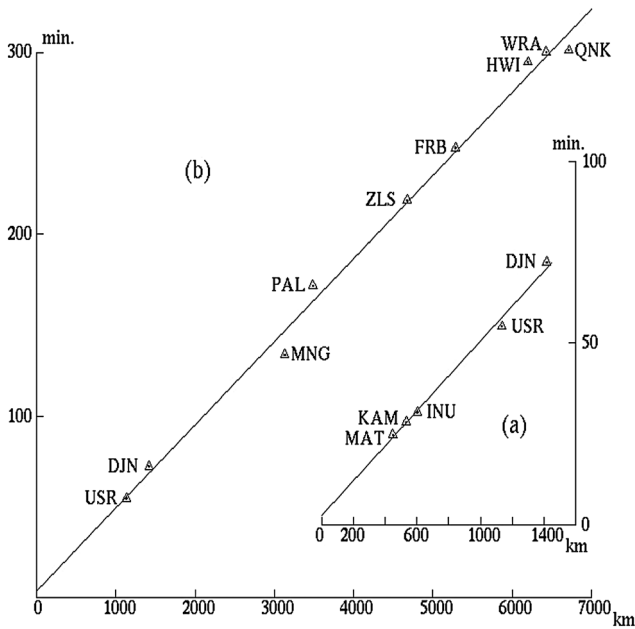


Figure 5. (a) Travel time–distance relation for the waves recorded at regional stations. The apparent phase velocity in the distance range between 447 and 1419 km is roughly estimated as about 341 m/s. (b) Travel time–distance relation for the waves recorded at global stations. The apparent phase velocity in the distance range between 1136 and 6715 km is roughly estimated as 364 m/s.

case because this appears physically more plausible and also in view of the calculated results from the latter case tested in our previous article [Mikumo *et al.*, 2008].

[16] The propagation of acoustic-gravity waves propagating in the atmosphere can be described by the atmospheric transfer function $A(\omega)\exp[-i\varphi_A(\omega)]$ [Harkrider, 1964], i.e.,

$$A(\omega) = A_{Aj}(\omega)k^{1/2}/\omega, \varphi_A(\omega) = \omega r_0/C_j(\omega) - \pi/4 \quad (1)$$

where $A_{Aj}(\omega)$ is the dynamic response of the atmosphere to a surface source and receiver, r_0 is the distance from the source to the receiver site, and $C_j(\omega)$ is the phase velocity, where j indicates different mode numbers of acoustic-gravity waves; S_0, S_1, S_2 , etc., are the fundamental mode and the first and second higher modes of acoustic waves, and G_0 and G_1 indicate the fundamental mode and the first higher mode of gravity waves, respectively. The calculated two functions $A_{Aj}(\omega)$ and $C_j(\omega)$ are shown in Figures S3 and S2. These functions are subject to minor fluctuations due to temperature variations and seasonal wind structures. The high apparent velocity observed at global distances (section 2.2) would correspond to the high velocity branches of acoustic S_0 and S_1 modes for periods between 2 and 4.5 min (see Figure S2), which indicates the sound velocity in the thermosphere at altitudes higher than 110 km. It is also to be mentioned that GR_0 has nearly flat spectral amplitudes over periods between 4.5 and 14 min and that S_0 covers the period range from 2 to 4.5 min [Harkrider, 1964] (see Figure S3). The band-pass filtering applied to both regional and global IMS data in section 2 was to extract these low-frequency acoustic-gravity waves. We can calculate here the Green's functions for these acoustic and gravity modes

separately and sum up to obtain the synthetic waveform from a point source to any station located at some distance. Its example is shown in Mikumo *et al.* [2008, Figure 3].

3.2. Assumed Source for the 2011 Earthquake

[17] In addition to the atmospheric transfer function described above, our next step is to incorporate earthquake source parameters and then calculate synthetic waveforms and compare them with the observed barograms. The parameters to be estimated or assumed are as follows: (1) the locations and dimensions of upheaval and depression of the sea surface due to the coseismically uplifted and subsided zones of the sea bottom, (2) the pattern and amount of vertical displacements in these subdivided zones, (3) the time constant or risetime of the deformation, and (4) the expanding velocity of the source region.

[18] The 2011 great thrust earthquake produced large-scale uplift and subsidence of the sea bottom over a wide area off the east coast of the Tohoku region. The rapid change of the sea bottom then generated upheaval and depression of the sea surface over this area, which caused high initial amplitude of tsunami. Previous theoretical studies [Kajiura, 1963, 1970] and recent numerical simulations [Saito and Furumura, 2009] show that if the wavelength of coseismic sea-bottom deformation is much longer than the water depth and if the deformation takes place within a few minutes, then the sea surface behaves almost exactly like the sea-bottom deformation. These conditions correspond exactly to the present case when the wavelength of the coseismic deformation is on the order of about 100–200 km, which is much longer than the water depth of about 8000 m beneath the source region off the Pacific coast, and also the duration of deformation may be on the order of a few minutes or a little bit longer.

[19] The source region generating high-amplitude tsunami has been directly or indirectly estimated from various types of tsunami observations, such as with coastal tide gauges, offshore ocean-bottom pressure gauges, telemetered GPS wave gauges, and so on, sometimes combined with the inland GPS network [e.g., Fujii *et al.*, 2011; Hayashi *et al.*, 2011; Maeda *et al.*, 2011; Sato *et al.*, 2011; Saito *et al.*, 2011]. In particular, the extent of the tsunami source region and the “initial” tsunami amplitude have been estimated by the waveform inversion of the various types of observations. The results appear to show that the large-amplitude tsunami region may be confined to the zone of approximately $250 \text{ km} \times 200 \text{ km}$ within the seismically estimated region of about $500 \text{ km} \times 250 \text{ km}$, and the maximum initial tsunami height reaches 8 m near the Japan Trench axis [Fujii *et al.*, 2011; Saito *et al.*, 2011]. As a first approximation, we refer to the tsunami source region in estimating the source area effectively exciting atmospheric pressure waves.

[20] Figure 6 simply depicts this assumed source region that could excite atmospheric pressure waves. Notations 1U, 2U, 3U, and 4U indicate tsunami upheaval zones, and 1D and 3D are tsunami depression zones, all of which are tentatively enclosed by rectangles, with L_1, L_2 , and L_3 and W_1 and W_2 as their lengths and widths to be estimated, respectively.

3.3. Dynamic Response of the Atmosphere

[21] If the initial upheaval and depression of the sea surface due to coseismic uplift and subsidence of the sea bottom is expressed as [Mikumo *et al.*, 2008]

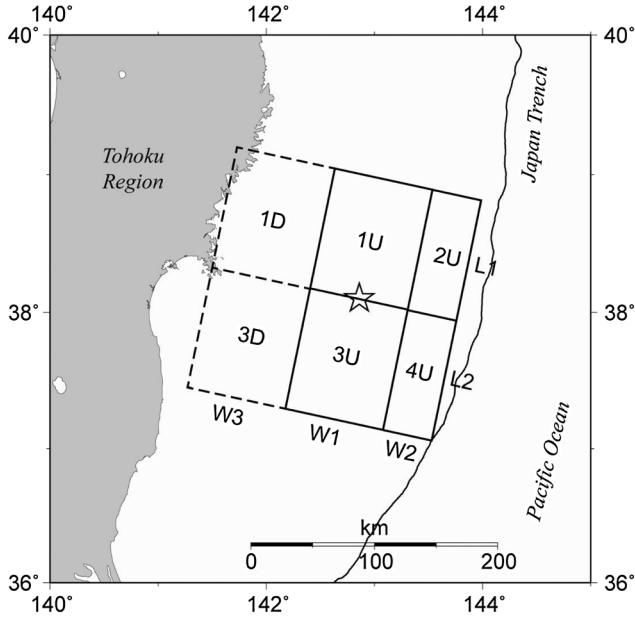


Figure 6. Assumed source regions exciting atmospheric pressure waves, referring to the tsunami source regions [Fujii *et al.*, 2011; Saito *et al.*, 2011]. $L1$ and $L2$ are assumed lengths, and $W1$, $W2$, and $W3$ are assumed widths, which enclose six subdivided source zones: 1U, 2U, 3U, and 4U indicate upheaval zones, and 1D and 3D indicate depression zones, respectively.

$$z_0(r, t) = (a/2) [1 - \cos(\pi t/\tau)] \quad (\text{for } t < \tau, r < Li, Wi) \quad (2)$$

where a and τ are the vertical displacement and its time constant, respectively. In this case, the upward particle velocity of the air w_0 at $z=0$ is equal to that of the sea surface $w_0 = dz_0/dt = (\pi a/2\tau)\sin(\pi t/\tau)$. The pressure perturbation p_0 just above there can be approximately given by $p_0 = \rho_0 c_0 w_0$ if the ratio of the time constant of the coseismic vertical displacement to the local Brunt period (~ 340 s) is less than 0.3 [Mikumo, 1968] and if the phase velocity of the expanding source is much faster than the sound velocity [Watada *et al.*, 2006], where ρ_0 and c_0 are the ambient air density and the sound velocity near the sea surface, respectively.

[22] In this case, the source spectrum $S(\omega)$ of the pressure perturbation p_0 is expressed as

$$S(\omega) = (\rho_0 c_0 a/2\tau) \sin(2\omega\tau) / [(\omega\tau/\pi)^2 - 1] \quad (3)$$

$$\varphi_S(\omega) = \exp(-i\omega\tau)$$

[23] When the source extends for the area $2Li \times 2Wi$, with its horizontal expanding velocity v , the source finiteness factor can be derived from integration of a point source solution (2), i.e.,

$$D(\omega) = 4LiWi \left\{ \frac{\sin(\omega T_{Li})}{(\omega T_{Li})} \right\} \left\{ \frac{\sin(\omega T_{Wi})}{(\omega T_{Wi})} \right\}$$

$$\varphi D(\omega) = \exp\{-i\omega(T_{Wi} + T_{Wi})\}$$

where $T_{Li} = Li [1/v - \cos\beta/C_j(\omega)]$ and $T_{Wi} = Wi [1/v - \sin\beta/C_j(\omega)]$. (4)

and v is the horizontal spreading velocity of the source area, and β is the azimuth from the source to the station with respect to the direction of bilateral source spreading [Mikumo *et al.*, 2008].

[24] Finally, if we assume a linear system coupled between the solid earth, the sea surface, and the atmosphere, the pressure perturbation that would be recorded at any station in the far field, compared with the source dimension and the wavelength, can be written in the frequency domain as

$$[p_0(r, 0, t)]_{Aj} = c(r/R \sin\theta)^{1/2} \int F(\omega) \exp\{-i\varphi(\omega)\} d\omega \quad (5)$$

$$F(\omega) = S(\omega)D(\omega)A(\omega)B(\omega)$$

$$\varphi(\omega) = \varphi_S(\omega) + \varphi_D(\omega) + \varphi_A(\omega) + \varphi_B(\omega)$$

where $S(\omega)$, $D(\omega)$, $A(\omega)$, and $B(\omega)$ are the source time spectrum, the source finiteness spectrum, the atmospheric transfer function defined as in equation (1), and the barograph response, respectively, and $\varphi(\omega)$ s are their phase spectra, respectively [Mikumo *et al.*, 2008]. Here $c = 2(2/\pi)^{1/2}$ is simply a numerical constant derived from Harkrider's formulations [1964], and $(r/R \sin\theta)^{1/2}$ is the approximate curvature correction for the effect of energy spreading over a spherical earth instead of a flat surface, with the distance r to the recording station from the source, the Earth's radius R , and the spherical colatitude of the station θ . It is now possible to calculate synthetic waveforms at any station and compare them with the observed records.

4. Comparison Between the Observed and Synthetic Barograms

4.1. Method

[25] It is shown in Figure 4 that there is some variability of observed waveforms among individual traces at some of the stations. We believe that the waveforms that deviated appreciably from the average features, particularly in the case involving higher frequencies, may be attributed to local site conditions. We focused our attention to their coherent low-frequency waveforms and selected any one trace not heavily disturbed by these higher-frequency components as representative of the recording at its station. We did not apply numerically averaging procedure over all the traces because this procedure would sometimes deform their original waveforms having some phase differences.

[26] For the source exciting atmospheric pressure waves, referring to the tsunami source region depicted in Figure 6, we fix the locations and subdivided zones as shown there with respect to the JMA epicenter (indicated by an asterisk). Because the shortest period involved in the filtered waveforms is around 2 min, the corresponding wavelength would be about 40 km. This implies that the minimum resolvable dimension of the subdivided zones from the observed atmospheric waveforms would be of this order, and hence, we take the dimensions of subdivided zones as larger than this in the following way: $L1 = 100\text{--}120$ km, $L2 = 100\text{--}120$ km, $W1 = 80\text{--}120$ km, $W2 = 50\text{--}80$ km, and $W3 = 80\text{--}100$ km. Under this situation, each source dimension within these ranges would not give important effects on the calculated far-field waveforms. The next parameter to be estimated is the vertical displacements in these zones, which are directly related to the amplitudes of synthetic waveforms. Our second step is to vary systematically each of the displacements by fixing the rest of the displacements and giving tentative values for each of the risetimes in eight possible models shown in Table 2. Through this procedure, we found the

Table 2. Estimated Source Parameters^a

Models	L1 (km)	L2 (km)	W1 (km)	W2 (km)	W3 (km)	D1U (m)	D3U (m)	D2U (m)	D4U (m)	D1D (m)	D3D (m)	T1U (min)	T3U (min)	T2U (min)	T4U (min)	T1D (min)	T3D (min)
Syn71	120	120	120		120	6.0	6.0			-1.0	-0.5	3.0	3.0			3.0	2.0
Syn72	120	120	120		120	6.0	6.0			-1.5	-1.0	4.0	4.0			3.0	2.0
Syn73	120	120	100		100	6.0	6.0			-1.5	-1.0	4.0	4.0			3.0	2.0
Syn81	120	120	120	50	100	6.0	6.0	6.0	6.0	-1.0	-0.5	4.0	4.0	3.0	3.0	3.0	2.0
Syn82	120	120	120	50	100	6.0	6.0	8.0	8.0	-1.5	-1.0	4.0	4.0	3.0	3.0	3.0	2.0
Syn83	120	120	100	50	100	6.0	6.0	8.0	8.0	-1.5	-1.0	4.0	4.0	2.0	2.0	3.0	2.0
Syn84	120	120	100	50	100	6.0	6.0	8.0	8.0	-1.5	-1.0	4.0	4.0	1.5	2.0	3.0	2.0
Syn91	120	120	100	50	100			8.0	8.0	-1.5	-1.0			4.0	4.0	3.0	2.0
Syn92	120	120	100	50	100			8.0	8.0	-1.5	-1.0			3.0	3.0	3.0	2.0
Syn93	120	120	100	50	100			8.0	8.0	-1.5	-1.0			2.0	2.0	3.0	2.0
Syn94	120	120	100	50	100			8.0	8.0	-1.5	-1.0			1.5	2.0	3.0	2.0

^aL1 and L2 are the lengths and W1, W2, and W3 are the widths of the subdivided zones, respectively (see Figure 6). D1U, D3U, D2U, and D4U indicate the average upheaval displacements at zones 1U, 3U, 2U, and 4U, and D1D and D3D indicate the average depression displacements at zones 1D and 3D, respectively. T1U, T3U, T2U, T4U, T1D, and T3D stand for risetimes τ , indicating the time constants at these zones, respectively.

possible range of the displacements ranging between 3 and 6 m for D1U and D3U and between 4 and 8 m for D2U and D4U for tsunami upheaval zones, and between -1 and -3 m for tsunami depression zones. The estimated values are found to be within the scope of the inversion results of tsunami data by *Fujii et al.* [2011] and *Saito et al.* [2011]. The latter results have been obtained directly for the sea surface, while the former results have been calculated for the slip distribution on a dipping fault and then transformed into the change of the sea bottom through a 3-D elastic dislocation theory (Okada, 1985) for this purpose. The third important parameter is the time constant or the risetime τ of the vertical displacements in equations (2) and (3). The time constant directly affects the synthetic waveforms and, hence, is most interesting. Likewise, after a large number of risetimes were systematically varied by fixing the remaining risetimes and taking the estimated displacements, we found the possible range of these values to be $\tau = 1.5\text{--}4.0$ min for the upheaval zones and 1–3 min for the depression zones, as shown in Table 2. By this forward modeling procedure, however, it is difficult to find a unique solution to obtain the best fit between the observed and synthetic waveforms simultaneously at all stations. This is an inherent problem in forward modeling techniques.

[27] The fourth parameter is the horizontal spreading velocity of the source area, as given in equation (4). We tested different cases with v ranging from 1 to 3 km/s, but the effects on the far-field waveforms are quite limited, as in the previous case [Mikumo et al., 2008]. For this reason, we fixed the velocity v to be 2.5 km/s. In all the following calculations for synthetic waveforms, we employed the forward modeling procedure, not any inversion techniques. This is because the numbers of stations are quite limited and the recorded waveforms are sometimes contaminated by unexpected ambient noise due to wind effects and so on.

4.2. Results

[28] 1. The first case is the IS07 Warramunga station located nearly southward at an epicentral distance of 6430 km. Figure 7a shows three synthetic waveforms Syn72, Syn92, and Syn81 with different initial amplitudes from 6 to 8 m and time constants from 3.0 to 4.0 min, as shown in Table 2. It is found that these three models provide quite reasonable agreement to the observations given in the uppermost trace, but with a rather longer period. The next three models are Syn93, Syn92, and Syn91 for different time

constants τ ranging from 2.0 to 4.0 min with an initial tsunami height of 8 m in two narrow zones U2 and U4 located near the trench axis. Comparing these synthetics with the recorded waveform, we notice in Figure 7b that Syn93 with $\tau = 2$ min gives better fit to the recorded waveform, while Syn92 with $\tau = 3$ min yields monochromatic waveforms, and Syn91 with $\tau = 4$ min provides a rather longer period. This comparison suggests that $\tau = 2$ min in the two zones U2 and U4 is most probable among these cases. Accordingly, we incorporate the source parameters in Syn93 into model Syn83, which includes two wider central zones U1 and U3. Figure 7c shows two synthetics from these two models Syn93 and Syn83, each having the same initial tsunami amplitude of 8 m and a time constant of $\tau = 2$ min in the U2 and U4 zones, as given in Table 2. The synthetics from these two models well reproduce the general features of the recorded waveforms.

[29] 2. The second case shown here is the IS59 Hawaii station located nearly due eastward at an epicentral distance of 6201 km facing directly the Japan Trench, where unexpectedly high amplitude tsunami have been observed. Accordingly, the initial amplitude and its risetime would most effectively affect the waveforms observed at this station. A number of possible different models, including Syn72, Syn82, and Syn92, have been tested (not shown here) to see these effects on the Hawaii waveforms. Among these models, Figure 8a shows the synthetic waveforms from two probable models, Syn93 and Syn83, both of which include the 2U and 4U zones with a high initial amplitude of 8 m and a relatively shorter risetime of 2 min, as for the case of the Warramunga station. Syn83 includes two central zones U1 and U3 with the initial height of 6 m with a time constant of 4 min, as shown in Table 2. The two cases provide almost equally, quite reasonable agreement to the observed waveforms, at least for a time interval of the initial 2100 s (about 35 min). Although it may be concluded that the two zones U2 and U4 provided strong effects to the observations at this station, another two central zones U1 and U3 behind these narrow zones also have physically important role to the observations at this station. A number of trial calculations also indicate that the parameters specifying the westward depression zones D1 and D3 do not give important effects on the synthetic waveforms at this station.

[30] 3. The third case is the IS53 Fairbanks station located northeastward at a distance of 5288 km, most of the traveling

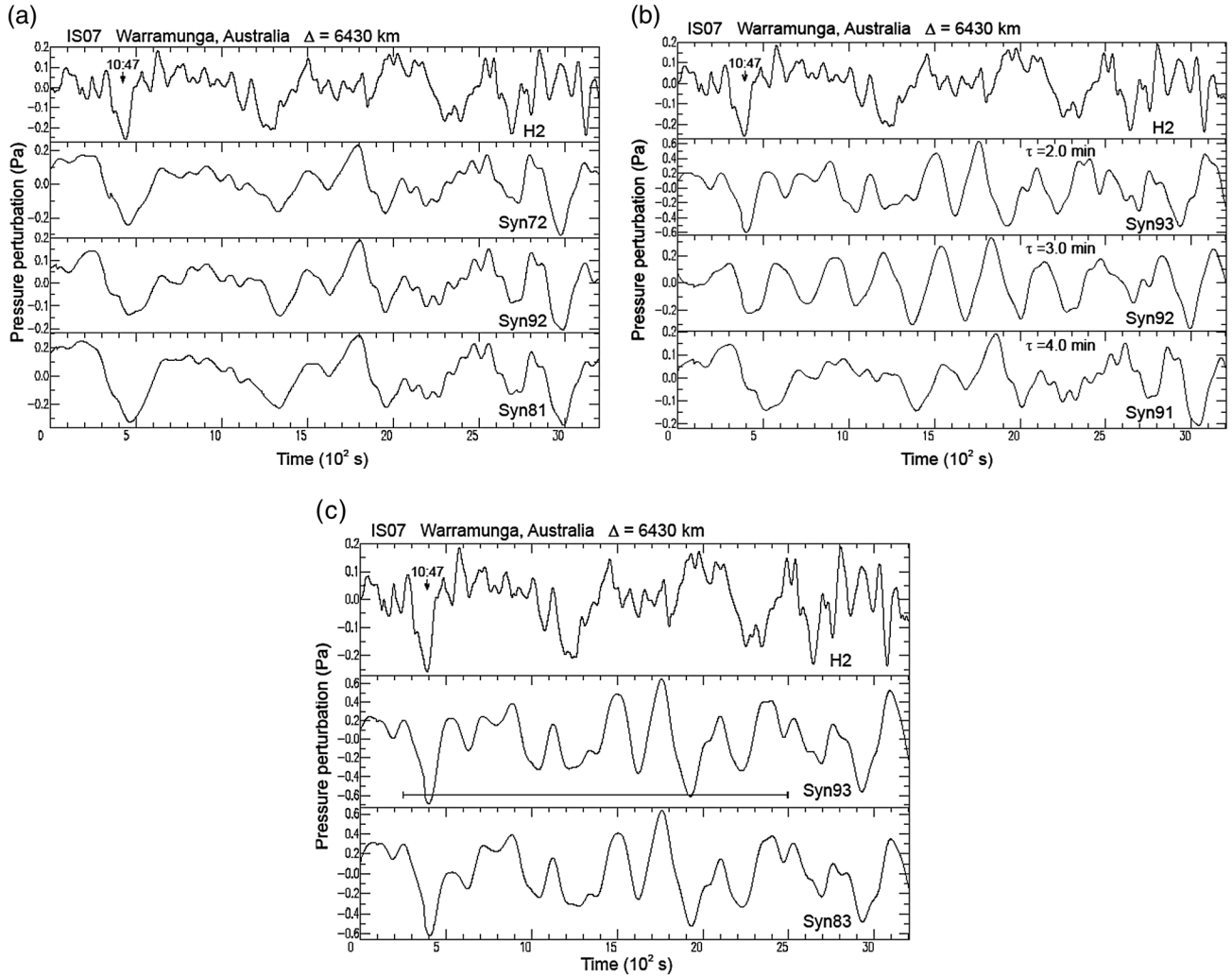


Figure 7. Comparison between the waveforms recorded at the IS07 Warramunga station and the synthetics for the three assumed parameters. (a) The uppermost trace indicates the recorded waveform H2 and the three synthetics for three different models Syn72, Syn92, and Syn81 given in Table 2. (b) The recorded waveform H2 and three synthetics with different time constants $\tau = 2.0, 3.0,$ and 4.0 min for models Syn93, Syn92, and Syn91, respectively. It can be seen that $\tau = 2.0$ min gives reasonable agreement between the recorded and synthetic waveforms. (c) The recorded waveform H2 and two synthetic waveforms from models Syn93 and Syn83.

path from the epicenter being over the Pacific Ocean. A number of possible models have been tested, and Syn81 and Syn84 provide synthetic waveforms that appear to show a limited agreement to the observed waveform (not shown here). It is found, however, that the two models Syn83 and Syn93, including the high amplitude and quite short risetime in the two zones 2U and 4U, provide better agreement between the synthetic and observed waveforms for the time interval of about 2100 s (35 min), as shown in Figure 8b. This is the same situation as for the Hawaii station. In this way, the observations at the above three stations located southward, eastward, and northeastward facing the Pacific Ocean side strongly suggest that the eastern zone of the source region has higher amplitude upheaval of the sea surface with quite shorter time constants than its western side. This agrees with the findings from tsunami observations.

[31] 4. A well-recorded waveform has been obtained at the IS18 Quanaak station located nearly northward at a largest

distance of 6716 km, as shown in Figure 4h. For comparison with the foregoing three stations, we also calculate two synthetic waveforms from Syn83 and Syn93 models, and it is found that the Syn83 model yields partially satisfactory agreement to the recorded waveform only for the first 15 min, as shown in Figure 8c. Further attempts have been made for another two cases, Syn84 and Syn94 with a shorter risetime of 1.5 min, or northward extending dimension by 50 km [Fujii and Satake, 2012], only for the northeastern zone U2 to improve the discrepancy. However, any of these modified models did not provide better fit to the observed waveforms (not shown here). As mentioned in section 2.2, the record lacks long periods but shows a waveform with periods shorter than 3.5 min. We tentatively assume here that the gravity modes do not propagate efficiently, but only the acoustic modes are predominant. Under this assumption, we construct a synthetic waveform as shown in the second trace as “Acoustic Syn71” in Figure 8d, where acoustic

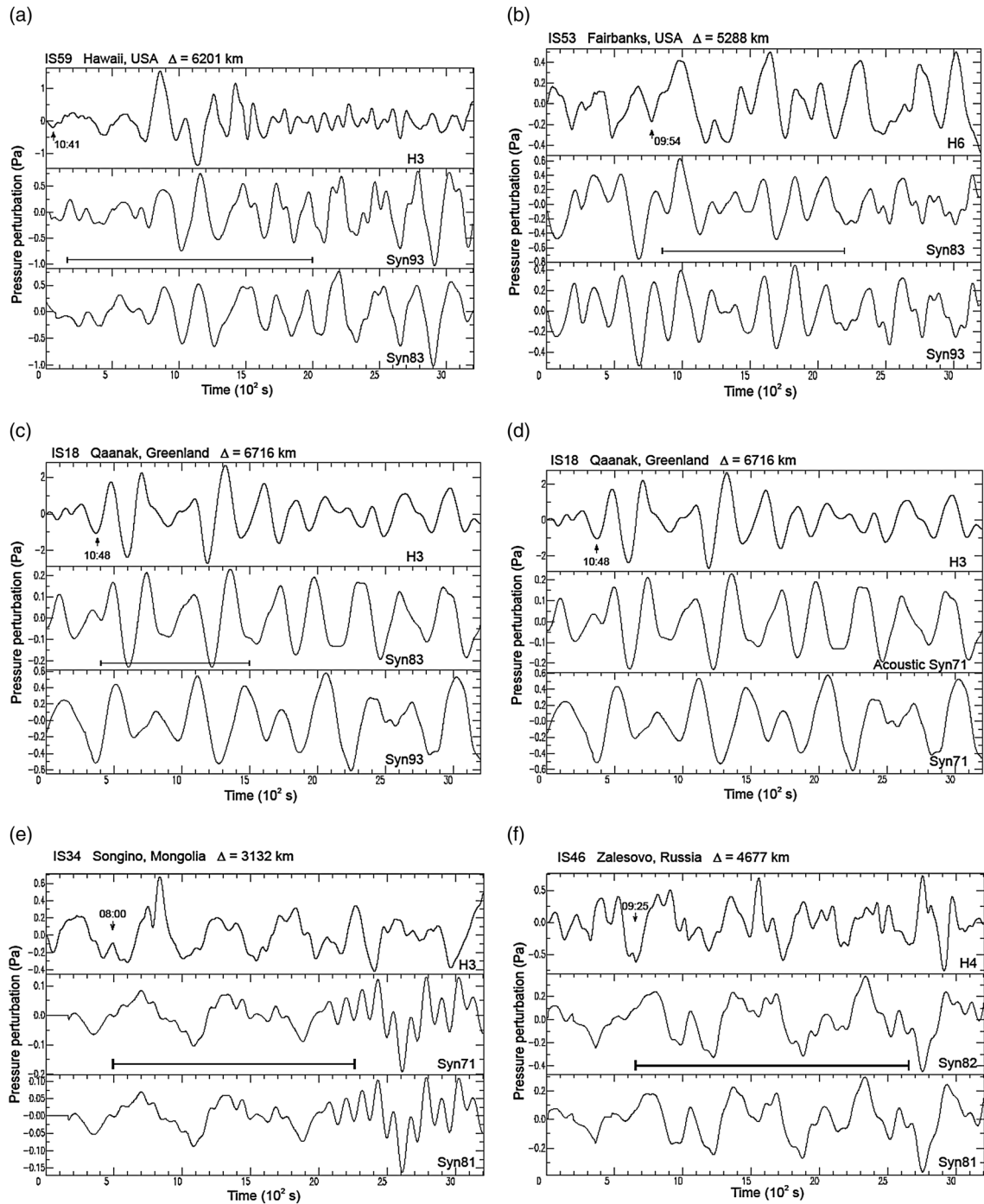


Figure 8. (a) Comparison between the waveform H3 recorded at the IS59 Hawaii station and two synthetics from two models Syn93 and Syn83. (b) Comparison between the waveform H6 recorded at the IS53 Fairbanks station and two synthetics Syn93 and Syn83. Reasonable fit may be seen only for the underlined time interval indicated by a horizontal line. (c) Comparison between the waveforms H3 recorded at the IS18 Qaanaq station and two synthetics Syn83 and Syn93. Reasonable agreement can be seen between the recorded and synthetic waveforms only for the first 25 min. (d) Comparison between the waveform H3 recorded at the IS18 Qaanaq station. AcousticSyn71 is of only acoustic modes and appears to give better fit to the recorded waveform for a time interval of the first 25 min, but with smaller amplitude than that of H3. Syn71, including both gravity and acoustic modes, does not provide good fit to the recorded waveform. (e) Comparison between the waveform H3 recorded at the IS34 Mongolia station with two synthetics Syn71 and Syn81. There is quite reasonable fit between the underlined time interval indicated by a horizontal line. (f) Comparison between the waveforms H4 recorded at the IS46 Zalesovo station and two synthetics Syn82 and Syn81. Quite reasonable fit between them may be noticed for the underline time interval indicated by a horizontal line.

modes S_0 , S_1 , and S_2 are included, while the third trace Syn71 includes both gravity and all acoustic modes. We notice that the first 1500 s (25 min) in “Acoustic Syn71” compares quite well with the recorded waveform but with a large difference between their absolute amplitudes, whereas Syn71 does not give a better agreement. There leaves a question, however, as to why gravity modes could not propagate efficiently to this station. This might be due to temperature or wind conditions in the lower to middle atmosphere along this propagation path. This still remains unanswered at this moment.

[32] 5. Figure 8e shows a comparison between the recorded and synthetic waveforms for the IS34 Mongolia station located northwestward at an epicentral distance of 3132 km. Models Syn71 and Syn81 appear to provide quite reasonable fit to the recorded waveform for the time interval of 1800 s (30 min) indicated by a horizontal line. It appears that the longer period signals of 6–8 min may be modeled to some extent.

[33] 6. Similar comparisons are made in Figure 8f for the IS46 Zolesovo station located also northwestward from the epicenter at a distance of 4678 km. It is noticed that for a time interval of about 2100 s (35 min), there is quite good fit between the recorded and synthetic waveforms for two models Syn82 and Syn81. For the above two stations located northwestward, similar calculations have been made for synthetic waveforms also from Syn83 and Syn93 with the high tsunami amplitude and the quite shorter risetime as for the previous four stations. However, comparisons between the synthetic and observed waveforms do not give better agreement in these cases (not shown here), suggesting that the unusual upheaval of the sea surface near the Japan Trench does not provide significant effects on these western stations, unlike the three stations located at the eastern side.

5. Tsunami Arrival

[34] After the arrival of acoustic-gravity waves, tsunami waves propagating over the Pacific Ocean arrived to Kawaihae on the Island of Hawaii after a travel time of ~ 7.8 h [Bressan and Tinti, 2012]. The tsunami speed in this case is estimated as 221 m/s, which would correspond to an average ocean depth of 5 km through the travel path. The time difference between the detected acoustic wave arrival and the tsunami arrival was ~ 2.6 h. This demonstrates that the acoustic arrival could be used as early tsunami warning in the case of future large events, as has been pointed out also in the case of shorter epicentral distances during this earthquake [Arai *et al.*, 2011].

6. Discussion and Conclusions

[35] It has been shown that low-frequency atmospheric waves were recorded at four regional stations and at eight global IMS stations within 5 h after the 2011 great Tohoku earthquake. The apparent phase velocity of the recorded waves ranged from 341 m/s at the regional distances up to 364 m/s at the global distances up to 6700 km. A comparison between the recorded waveforms with the synthetics expected from a large number of calculations with various source properties shows that these waves may be interpreted as the acoustic-gravity waves excited by high-amplitude upheaval and depression of the sea surface due to coseismic

uplift and subsidence of the sea bottom caused by the large-scale thrust earthquake and propagated through the lower to the middle atmosphere. At a few stations, however, the recorded waveforms are disturbed by prevailing atmospheric and ambient instrumental conditions, and hence, it is not always easy to compare the recorded amplitudes exactly with those expected from their corresponding calculations. The pressure perturbation expected at the tsunami source region ranges from several to a few tens of pascals for low-frequency waves if we assume their related parameters as $\rho_0 = 1.239 \times 10^{-3}$ g/cm³, $c_0 = 320$ m/s, and $w_0 = 6$ m/4 min to 8 m/2 min. In addition, there could be some wave attenuation and fluctuation in spectral amplitudes due to thermal and seasonal wind structures in the lower to middle atmosphere, which could deviate real atmospheric conditions at the time of the earthquake from the assumed standard structure. For this reason, we did not make further discussion on this point.

[36] The synthetic waveforms are generally consistent with the overall features of the observed low-frequency acoustic-gravity waves, at least for the initial time interval of 25–40 min. The observations at three stations located due eastward, southward, and northeastward facing the Pacific Ocean side strongly suggest that the eastern zone of the source region adjacent to the Japan Trench has significantly higher-amplitude, initial upheaval of the sea surface probably up to 8 m with quite shorter time constant down to 2 min. This essentially agrees with the findings from tsunami waveform inversions [Fujii *et al.*, 2011; Saito *et al.*, 2011] based on various types of tsunami observations. It may be also concluded that the average coseismic upheaval beneath the central zone of the tsunami source region may exceed 4–6 m and that the time constant of the tectonic deformation may be in the range between 3 and 4 min, which is the time elapsed shortly before generating tsunami waves. The estimated average time constant is significantly longer than that in the 1968 Alaskan [Mikumo, 1968] and the 2004 Sumatra-Andaman [Mikumo *et al.*, 2008] earthquakes.

[37] There leaves another problem that the waveforms recorded at a northernmost Greenland station did not involve much of lower-frequency waves as those at other IMS stations but nevertheless retained higher amplitudes. A part of the records at this station could be explained partially by the arrival of only acoustic modes, but its physical mechanism still remains unanswered at this moment.

[38] It has been also shown that the acoustic wave arrival could be used as an early tsunami warning system in the future, as has been demonstrated in the comparison between the two different arrivals at the Hawaii station.

[39] **Acknowledgments.** We thank the CTBTO for providing us with the IMS data obtained at several stations. The observations at Daejeon, Korea, are being operated by JAMSTEC with the support of the Korean Institute of Geosciences and Mineral Resources (KIGAM). We are grateful to an anonymous reviewer for his constructive review of the present manuscript and also to the Editor of this paper. Our thanks are extended to Nobuo Arai and Shingo Watada for some discussion at an early stage of this study.

References

- Ammon, C. J., T. Lay, J. Charles, H. Kanamori, and M. Cleaveland (2011), A rupture model of the great 2011 Tohoku earthquake, *Earth Planets Space*, 63, 693–695.
- Arai, N., M. Iwakuni, S. Watada, Y. Imanishi, T. Murayama, and M. Nogami (2011), Atmospheric boundary waves excited by the tsunami

- generation related to the 2011 great Tohoku-Oki earthquake, *Geophys. Res. Lett.*, *38*, L00G18, doi:10.1029/2011GL049146.
- Bolt, B. A. (1964), Seismic air waves from the great Alaskan earthquake, *Nature*, *202*, 1095–1096, doi:10.1038/2021095a0.
- Bressan, L., and S. Tinti (2012), Detecting the 11 March 2011 Tohoku tsunami arrival on sea-level records in the Pacific Ocean: Application and performance of the Tsunami Early Detection Algorithm (TEDA), *Nat. Hazards Earth Syst. Sci.*, *12*, 1583–1606, doi:10.5194/nhess-12-1583-2012.
- Drob, D. P., J. M. Picone, and M. A. Garces (2003), The global morphology of infrasound propagation, *Geophys. Res. Lett.*, *108*. doi:10.1029/2002JD003307.
- Fujii, Y., K. Satake, S. Sakai, M. Shinohara, and T. Kanazawa (2011), Tsunami source of the 2011 off the Pacific coast of Tohoku earthquake, *Earth Planets Space*, *63*, 815–820.
- Fujii, Y. and K. Satake (2012), Multiple time-window tsunami waveform inversion of the 2011 off the Pacific coast of Tohoku earthquake, Annu. Meet. Seismol. Soc. Jpn., 2012, P2-69.
- Garcés, M. A., P. Caron, C. Hetzer, A. Le Pichon, H. Bass, D. Drob, and J. Bhattacharyya (2005), Deep infrasound radiated by the Sumatra earthquake and tsunami, *Eos*, *86*(35), 30 August 2005.
- Garcés, M. A., A. Perttu, and B. Williams (2011), Infrasonic troposphere-ionosphere coupling in Hawaii, *Eos Trans. AGU*, Fall Meet. Suppl., Abstract SA-23A-1897.
- Gusman, R. A., Y. Tanioka, S. Sakai, and H. Tsushima (2012), Source model of the 2011 Tohoku tsunami estimated from tsunami waveforms and crustal deformation data, submitted to *Earth Planet. Sci. Lett.*
- Harkrider, D. G. (1964), Theoretical and observed acoustic-gravity waves from explosive sources in the atmosphere, *J. Geophys. Res.*, *69*, 5295–5321. doi:10.1029/JZ069i024p05295.
- Hayashi, Y., H. Tsushima, K. Hirata, K. Kimura, and K. Maeda (2011), Tsunami source of the 2011 off the Pacific coast of Tohoku earthquake determined from tsunami arrival times at offshore observation station, *Earth Planets Space*, *63*, 809–913.
- Hedin, A. E. (1991), Extension of the MSIS thermospheric model into the middle and lower atmosphere, *J. Geophys. Res.*, *69*, 1159–1172. doi:10.1029/90JA02125.
- Ide, S., A. Baltay, and G. C. Beroza (2011), Shallow dynamic overshoot and energetic deep structure in the M_w 9.0 Tohoku-Oki earthquake, *Science*, *332*, 1426–1429. doi:10.1126/science.1207020.
- Kajiura, K. (1963), The leading wave of tsunami, *Bull. Earthquake Res. Inst. Univ. Tokyo*, *41*, 535–571.
- Kajiura, K. (1970), Tsunami source, energy and the directivity of wave radiation, *Bull. Earthquake Res. Inst. Univ. Tokyo*, *48*, 835–869.
- Koketsu, K., Y. Yokota, N. Nishimura, Y. Yagi, S. Miyazaki, K. Satake, Y. Fujii, H. Miyake, S. Sakai, Y. Yamanaka, and T. Okada (2011), A unified source model for the 2011 Tohoku earthquake, *Earth Planet Sci. Lett.*, *310*, 480–487.
- Lay, T., Y. Yamazaki, C. J. Ammon, K. F. Cheung, and H. Kanamori (2011), The great 2011 off the Pacific coast of Tohoku (M_w 9.0) earthquake: Comparison of deep-water tsunami signals with finite-fault rupture model predictions, *Earth Planets Space*, *63*, 797–801. doi:10.5047/esp2011.05.037.
- Lee, S. J., B. S. Huang, M. Ando, H. C. Chiu and J. H. Wang (2011), Evidence of large scale repeating slip during the 2011 Tohoku-Oki earthquake, *Geophys. Res. Lett.*, *38*, L19306, doi:10.1029/2011GL09580.
- Le Pichon, A., E. Blanc, and A. Hauchcorne (Eds) (2010), *Infrasound Monitoring for Atmospheric Studies*, Springer, New York, pp. 735.
- Lognonné, P. (2010), Seismic waves from atmospheric sources and atmospheric/ionospheric signatures, in *Infrasound Monitoring for Atmospheric Studies*, edited by A. Le Pichon, E. Blanc, and A. Hauchcorne, pp. 281–304, Springer, New York.
- Maeda, T., T. Furumura, S. Sakai, and M. Shinohara (2011), Significant tsunami observed at ocean-bottom pressure gauges during the 2011 off the Pacific coast of Tohoku earthquake, *Earth Planets Space*, *63*, 803–808.
- Mikumo, T. (1968), Atmospheric pressure waves and tectonic deformation associated with the Alaskan earthquake of March 28, 1968, *J. Geophys. Res.*, *73*, 2009–2025, doi:10.1029/JB073i006p02009.
- Mikumo, T., T. Shibutani, A. Le Pichon, M. Garces, D. Fee, T. Tsuyuki, S. Watada, and W. Morii (2008), Low-frequency acoustic-gravity waves from coseismic vertical deformation associated with the 2004 Sumatra-Andaman earthquake ($M_w=9.2$), *J. Geophys. Res.*, *113*, B12402, doi:10.1029/2008JB005710.
- Okada, Y. (1985), Surface deformation due to shear and tensile faults in a half-space, *Bull. Seismol. Soc. Am.*, *75*, 1135–1154.
- Pfeffer, R. L., and J. Zarichny (1963), Acoustic-gravity waves propagation in an atmosphere with two sound channels, *Pure Appl. Geophys.*, *55*, 175–199, doi:10.1007/BF02011231.
- Press, F., and D. G. Harkrider (1962), Propagation of acoustic-gravity waves in the atmosphere, *J. Geophys. Res.*, *67*, 3889–39008. doi:10.1029/JZ067i010p03889.
- Saito, T. and T. Furumura (2009), Three dimensional simulation of tsunami generation and propagation: Application to intraplate events, *J. Geophys. Res.*, *114*, B02307, doi:10.1029/2007JB005523.
- Saito, T., Y. Ito, D. Inazu, and R. Hino (2011), Tsunami source of the 2011 Tohoku-Oki earthquake, Japan: Inversion analysis based on dispersive tsunami simulations, *Geophys. Res. Lett.*, *38*, L00G19, doi:10.1029/2011GL049089.
- Sato, M., T. Ishikawa, N. Ujihara, S. Yoshida, M. Fujita, M. Mochizuki, and A. Asada (2011), Displacement above the hypocenter of the 2011 Tohoku-Oki earthquake, *Science*, *332*(6038), 1395–1397 doi:10.1126/science.1207401.
- Wares, G. W., K. W. Champion, H. L. Pond, and A. E. Cole (1960), Model atmosphere, in *Handbook of Geophysics*, pp. 1-1–1-37, Macmillan, N. Y.
- Watada, S., T. Kunugi, K. Hirata, H. Sugioka, K. Nishida, S. Sekiguchi, J. Oikawa, Y. Tsujii, and H. Kanamori (2006), Atmospheric pressure change associated with the 2003 Tokachi-Oki earthquake, *Geophys. Res. Lett.*, *33*, L24306, doi:10.1029/2006GL027967.
- Watada, S. (2009), Radiation of acoustic and gravity waves and propagation of boundary waves in the stratified fluid from a time-varying bottom boundary, *J. Fluid Mech.*, *627*, 367–377.
- Watada, S. and H. Kanamori (2010), Acoustic resonant oscillations between the atmosphere and the solid earth during the 1991 Mt. Pinatubo eruption, *J. Geophys. Res.*, *115*, B12319, doi:10.1029/2012JB007747.
- Yagi, Y. and Y. Fukahata (2011), Rupture process of the 2011 Tohoku-oki earthquake and absolute elastic strain release, *Geophys. Res. Lett.*, *38*, L19307, doi:10.1029/2011GL048701.
- Yeh, K. C., and C. H. Liu (1974), Acoustic-gravity waves in the upper atmosphere, *Rev. Geophys. Space Phys.*, *12*, 193–216. doi:10.1029/RG12i002p00193.
- Yoshida, Y., H. Ueno, D. Muto, and S. Aoki (2011), Source process of the 2011 off the Pacific coast of Tohoku earthquake with the combination of teleseismic and strong motion data, *Earth Planets Space*, *63*, 565–569.